

E-XQR-30: Evidence for an Increase in the Ionization State of Metal Absorbers from $z \sim 6$ to $z \sim 2$

Stephanie Rowlands,^{1,2} R. L. Davies,^{1,2} E. Ryan-Weber,^{1,2} L. C. Keating³, A. M. Sebastian,^{1,2} G. D. Becker,⁴ M. Bischetti,^{5,6} S. E. I. Bosman^{7,8}, H. Chen,⁹ F. B. Davies,⁸ V. D’Odorico,^{6,10} P. Gaikwad,¹¹ S. Gallerani,¹² M. G. Haehnelt,^{13,14} G. Kulkarni,¹⁵ R. A. Meyer,¹⁶ L. Welsh,^{17,6} Y. Zhu¹⁸

¹Centre for Astrophysics and Supercomputing, Swinburne University of Technology, Hawthorn, Victoria 3122, Australia

²ARC Centre of Excellence for All Sky Astrophysics in 3 Dimensions (ASTRO 3D), Australia

³Institute for Astronomy, University of Edinburgh, Blackford Hill, Edinburgh EH9 3HJ, UK

⁴Department of Physics & Astronomy, University of California, Riverside, CA 92521, USA

⁵Dipartimento di Fisica, Università di Trieste, Sezione di Astronomia, Via G.B. Tiepolo 11, I-34131 Trieste, Italy

⁶INAF – Osservatorio Astronomico di Trieste, Via G.B. Tiepolo, 11, I-34143 Trieste, Italy

⁷Institute for Theoretical Physics, Heidelberg University, Philosophenweg 12, D-69120, Heidelberg, Germany

⁸Max-Planck-Institut für Astronomie, Königstuhl 17, D-69117 Heidelberg, Germany

⁹Augustana Campus, University of Alberta, Camrose, AB T4V2R3, Canada

¹⁰IFPU – Institute for Fundamental Physics of the Universe, via Beirut 2, I-34151 Trieste, Italy

¹¹Department of Astronomy, Astrophysics and Space Engineering, Indian Institute of Technology Indore, Simrol, MP 453552, India

¹²Scuola Normale Superiore, Piazza dei Cavalieri 7, I-56126 Pisa, Italy

¹³Institute of Astronomy, University of Cambridge, Madingley Road, Cambridge CB3 0HA, UK

¹⁴Kavli Institute for Cosmology, University of Cambridge, Madingley Road, Cambridge CB3 0HA, UK

¹⁵Tata Institute of Fundamental Research, Homi Bhabha Road, Mumbai 400005, India

¹⁶Department of Astronomy, University of Geneva, Chemin Pegasi 51, 1290 Versoix, Switzerland

¹⁷Centre for Extragalactic Astronomy, Durham University, South Road, Durham DH1 3LE, UK

¹⁸Steward Observatory, University of Arizona, 933 North Cherry Avenue, Tucson, AZ 85721, USA

Accepted XXX. Received YYY; in original form ZZZ

ABSTRACT

We investigate the evolution of the ionization state of metal-enriched gas in and around galaxies near the epoch of reionization using a sample of 488 metal absorption systems at $4.3 \lesssim z \lesssim 6.3$ from the E-XQR-30 survey. We classify the absorption systems based on whether they display only low-ionization absorption (C II, Si II, Mg II), only high-ionization absorption (C IV, Si IV), or both. The percentage of low-ionization-only systems decreases from 24% at $z \sim 6$ to 2% at $z \sim 4.3$, whilst the fraction of high-ionization-only systems increases from 52% to 82%. For mixed absorbers (with both low and high ionization absorption), we use the column density ratios $\log(N_{\text{CII}}/N_{\text{CIV}})$ and $\log(N_{\text{SiII}}/N_{\text{SiIV}})$ to quantify the average ionization as a function of redshift. The $\log(N_{\text{SiII}}/N_{\text{SiIV}})$ ratio does not change significantly over $5 \lesssim z \lesssim 6.3$. We combine the E-XQR-30 $\log(N_{\text{CII}}/N_{\text{CIV}})$ measurements with literature measurements at $z \sim 2–4$ and find that the $\log(N_{\text{CII}}/N_{\text{CIV}})$ ratio declines by a factor of ~ 20 between $z \sim 6$ and $z \sim 2$. To explore possible drivers of this evolution, we run photoionization models of gas slabs illuminated by a uniform UV background at fixed density, metallicity and H I column density. We find that the increase in the ionization state of metal absorbers towards lower redshifts can likely be explained by some combination of 1) an increase in the metallicity of C IV-absorbing gas and 2) a decrease in the typical H I column densities of the absorbing gas, driven by the declining cosmic mean density and a rapid rise in the strength of the UV background during the final stages of reionization.

Key words: intergalactic medium – galaxies: high-redshift – quasars: absorption lines – dark ages; reionization; first stars

1 INTRODUCTION

The Epoch of Reionization (EoR) is a transitional period impacting almost every baryon, during which the intergalactic medium went from a neutral state opaque to hydrogen ionizing photons to a transparent ionized state (Mesinger & Furlanetto 2009; Kollmeier

et al. 2014; McQuinn 2016; Carroll & Ostlie 2017). Constraining the sources of reionization as well as the exact timescale of when and how rapidly reionization occurred are topics of ongoing research (Becker et al. 2015a,b; McQuinn 2016; Fan et al. 2023; Qin et al. 2024). Neutral hydrogen gas absorbs ionizing photons, preventing direct measurements of the ionizing photon production rate and escape fraction from galaxies prior to the end of reionization. Recently, observations of Ly α emitters with JWST have provided unique constraints on the sizes and distributions of ionized bubbles as far back as

* E-mail: stephanierowlands@swin.edu.au

† E-mail: rdavies@swin.edu.au

$z \simeq 13$, supporting a scenario where reionization is primarily driven by faint, numerous star-forming galaxies (e.g. [Mason et al. 2025](#); [Runnholm et al. 2025](#); [Witstok et al. 2025](#)).

Absorption systems detected against the bright continuum of distant quasars provide a complementary and powerful probe of the properties of the intergalactic and circumgalactic medium during the epoch of reionization ([Fan et al. 2006](#); [Becker et al. 2015a](#); [Péroux & Howk 2020](#)). Studies of the Ly α forest and dark gap statistics have revealed that reionization was inhomogeneous and ended late ([Becker et al. 2001](#); [Ryden 2017](#); [Zhu et al. 2021, 2022](#); [Bosman et al. 2022](#)), with a recent forward modeling study constraining the end of the EoR to $z = 5.44 \pm 0.02$ ([Qin et al. 2024](#)).

Metal absorbers can be detected deep into the EoR and measuring the relative strengths of ions with significantly different ionization potentials offers a direct probe of the UV background (UVB) in the early Universe ([Pallottini et al. 2014](#); [Finlator et al. 2016](#); [Doughty et al. 2018](#)). High ionization species such as C iv and Si iv primarily trace warm, diffuse (10^5 K) gas in the circumgalactic medium (CGM), whereas neutral and low ionization species such as C ii and Si ii typically trace patches of colder (10^4 K), denser gas (see [Tumlinson et al. 2017](#), for a review).

Large surveys of metal absorption systems over cosmic time have revealed that the incidence of high-ionization C iv 1548,1550 \AA absorption grows rapidly from $z \sim 6$ to $z \sim 5$ (increasing by a factor of 2–4) and then increases more gradually from $z \sim 5$ to $z \sim 1.5$ ([Songaila 2001](#); [Becker et al. 2009](#); [Ryan-Weber et al. 2009](#); [Simcoe et al. 2011](#); [D'Odorico et al. 2013](#); [Boksenberg & Sargent 2015](#); [Bosman et al. 2017](#); [Codoreanu et al. 2018](#); [Meyer et al. 2019](#); [D'Odorico et al. 2022](#); [Davies et al. 2023b](#); [Anand et al. 2025](#)). Similar trends are seen in the Si iv 1393,1402 \AA number density ([Codoreanu et al. 2018](#); [D'Odorico et al. 2022](#)). In contrast, the incidence of neutral O i 1302 \AA and C ii 1334 \AA absorption decreases from $z \sim 6$ to $z \sim 5.5$ ([Becker et al. 2019](#); [Sebastian et al. 2024](#)), whilst the number densities of medium and weak Mg ii 2796,2803 \AA absorption remain approximately constant ([Sebastian et al. 2024](#)). The metallicity of the CGM increases towards low redshifts as a result of chemical enrichment by star-formation (e.g. [Madau & Dickinson 2014](#); [Deepak et al. 2025](#)). The marked decrease in O i and C ii between $z \sim 6$ and $z \sim 5.5$ thus points towards an increase in the ionization state of the absorbing gas, consistent with the rapid rise in high-ionization absorption over the same redshift range. This increase in ionization state may be driven by an increase in the strength and/or hardness of the ionizing photon background near the end of the EoR ([Becker et al. 2019](#); [Davies et al. 2023b](#)).

The change in ionization state can be directly examined by comparing the column densities of ions with substantially different ionization potentials. [D'Odorico et al. \(2013\)](#) found that the column density ratio of Si iv (with an ionization potential of 33.5 eV) relative to C iv (47.9 eV) decreases from $z \sim 5$ towards low redshift, suggesting an increase in the ionization state of the absorbing gas. However, the $N_{\text{SiIV}}/N_{\text{CIV}}$ ratio is also sensitive to variations in the relative abundances of carbon and silicon. Comparing different ions of the same element, such as C iv and C ii (11.3 eV), removes this systematic uncertainty. [Cooper et al. \(2019\)](#) compared the properties of low-ionization and high-ionization absorption in 69 intervening absorption systems at $z > 5$ observed with Magellan/FIRE and found evidence for a sharp decline in the $N_{\text{CII}}/N_{\text{CIV}}$ ratio from $z \sim 6$ to $z \sim 5.5$, which they suggest could be driven by a rapid increase in either the strength/hardness of the UV background or the metallicity of the diffuse C iv-absorbing gas. However, the majority of the absorption systems studied in [Cooper et al. \(2019\)](#) were detected in only one of C ii or C iv, meaning that only upper or lower limits

on the $N_{\text{CII}}/N_{\text{CIV}}$ ratio could be obtained. This makes it difficult to robustly measure how the average ratio changes with redshift.

Here, we further investigate the ionization properties of metal absorption systems near the end of the EoR using a sample of 488 metal absorbers from the enlarged Ultimate XSHOOTER legacy survey of quasars at $z \sim 5.8 - 6.6$ (E-XQR-30). This survey obtained deep observations at a spectral resolution of $R \simeq 10,000$, providing the largest homogeneous catalog of metal absorbers at $z > 5$ ([Davies et al. 2023a](#)). The E-XQR-30 catalog is a factor of three deeper than the [Cooper et al. \(2019\)](#) dataset and contains more than twice as many absorption systems at $z > 5$. The large sample enables us to separately investigate the evolution of systems showing only high-ionization species, only low-ionization species, and systems showing a mix of both. Focusing on C ii, C iv, Si ii and Si iv, we explore how the fraction of low-ionization, high-ionization and mixed absorption systems varies as a function of redshift. For systems with detections of both low-ionization and high-ionization absorption, we quantify the redshift evolution in the column density ratios $N_{\text{CII}}/N_{\text{CIV}}$ and $N_{\text{SiII}}/N_{\text{SiIV}}$. The E-XQR-30 measurements of the carbon and silicon ions span $4.3 < z < 6.5$ and $4.9 < z < 6.5$, respectively, covering the tail end of the EoR. We expand the measurements of $N_{\text{CII}}/N_{\text{CIV}}$ to lower redshifts by using data for absorption systems at $2 < z < 4$ from [Boksenberg & Sargent \(2015\)](#).

We describe the E-XQR-30 survey with the absorber sample and the calculation of column density ratios and absorber fractions in Section 2. Our results on the redshift evolution of metal absorber properties are presented in Section 3. We discuss comparisons to CLOUDY models and the implications for reionization in Section 4 and present our conclusions in Section 5.

2 SAMPLES AND DATA ANALYSIS

2.1 E-XQR-30 Sample

Our primary sample is drawn from the E-XQR-30 metal absorber catalogue ([Davies et al. 2023a](#)). E-XQR-30 is a deep spectroscopic survey of 42 of the brightest quasars at $z \sim 5.8 - 6.6$ ([D'Odorico et al. 2023](#)) with absolute magnitudes of $-27.8 < M_{1450\text{\AA}} < -26.2$ ([Bischetti et al. 2022](#)), designed to study quasars, enriched gas and the Lyman- α forest during the first billion years of the Universe. The survey represents the most extensive collection of high-quality spectra of early Universe quasars. The observations were conducted using VLT/X-Shooter which has 3 spectroscopic arms that together cover near-ultraviolet to near-infrared wavelengths from 3000 – 24800 \AA ([Vernet et al. 2011](#)). The E-XQR-30 spectra have a median spectral resolution of 11400 in the VIS arm and 9800 in the NIR arm and a median SNR of 30 per 10 km/s spectral channel ([D'Odorico et al. 2023](#)).

The metal absorption systems were cataloged as described in [Davies et al. \(2023a\)](#). An initial list of candidate systems was generated by performing an automated search for Mg ii, Fe ii, C ii, C iv, Si iv, and/or N v 1238,1242 \AA absorption. The candidates were filtered using a combination of automated algorithms and visual inspection. The Ly α forest is saturated at these redshifts, and therefore only the wavelength regions redward of the quasar Ly α emission line were searched. Table 1 shows the complete redshift range over which each ion can theoretically be detected when combining the data from all 42 quasars. Absorption components separated by less than 200 km s^{-1} were grouped into systems with column density given by the sum of the column densities of the constituent components. The full E-XQR-30 catalog contains 778 absorption systems over a redshift range of

Ion	Ionization energy (eV)	Redshift Range	Number of systems
C II 1334 Å	11.3	5.17 – 6.34	21
C IV 1548,1550 Å	47.9	4.34 – 6.34	444
Si II 1526 Å	8.2	4.42 – 6.34	21
Si IV 1393,1402 Å	33.5	4.94 – 6.34	85
Mg II 2796,2803 Å	7.6	2.04 – 6.34	90

Table 1. List of carbon, silicon and magnesium ions used in this study and their respective ionization potential energies (Kramida et al. 2024), along with the detectable redshift range from the E-XQR-30 spectra and the number of E-XQR-30 absorption systems with detections.

$2 \leq z \leq 6.5$ (Davies et al. 2023a). The E-XQR-30 catalog has a 50% completeness limit of $\log(N_{\text{CIV}}/\text{cm}^{-2}) = 13.2$, and therefore the absorption systems studied in this work most likely probe CGM gas. D’Odorico et al. (2016) showed that $\log(N_{\text{CIV}}/\text{cm}^{-2}) > 12$ corresponds to the CGM of galaxies at $z \sim 3$, and $z \sim 6$ C IV absorbers with $\log(N_{\text{CIV}}/\text{cm}^{-2}) > 13 – 13.5$ have associated galaxies within 200 pkpc (Díaz et al. 2021; Kashino et al. 2023).

2.2 Carbon and Silicon Absorber Properties

To determine whether the ionization state of the CGM changes with redshift, we focus on the singly ionized and triply ionized states of carbon (C II and C IV) and silicon (Si II and Si IV). The doubly ionized ions of carbon and silicon, C III 977 Å and Si III 1206 Å, could not be used because they fall in the Ly α forest. Four strong Si II lines fall within the wavelength range of the E-XQR-30 spectra: 1260 Å, 1304 Å, 1526 Å, and 1808 Å. Si II 1260 Å is the strongest line but is only detectable at $5.5 \lesssim z \lesssim 6.3$. The second strongest line, Si II 1526 Å, is six times weaker but detectable over a significantly larger redshift range, $4.4 \lesssim z \lesssim 6.3$. If we were to use both Si II 1260 Å and Si II 1526 Å at $z \gtrsim 5.5$ and only Si II 1526 Å at lower redshifts, the 50% completeness limit for Si II detection would be 6× deeper in the highest redshift interval, making it difficult to interpret potential variations in the ionization state of silicon absorbers as a function of redshift. Therefore, we exclusively use Si II 1526 Å because it provides the best compromise between oscillator strength and redshift range.

We select absorption systems containing any of the C II, C IV, Si II and Si IV metal absorption lines, with no restrictions in column density. We restrict our sample to systems at redshifts where both ions of either carbon or silicon fall redward of the quasar Ly α line and outside of masked spectral regions (Davies et al. 2023a). This results in a sample of 172 systems (after grouping components within 200 km s $^{-1}$). We further restrict the sample to intervening absorbers (at least 10,000 km/s below the quasar redshift) to avoid absorption systems potentially impacted by the strong quasar radiation field (e.g. Berg et al. 2016; Perrotta et al. 2016) or heating due to quasar-driven winds (e.g. Bischetti et al. 2022; Bischetti et al. 2023). This leaves a total sample of 148 systems.

We use the column density ratios $\log(N_{\text{CII}}/N_{\text{CIV}})$ and $\log(N_{\text{SiII}}/N_{\text{SiIV}})$ as proxies for the ionization state of the absorbing gas. If both ions of silicon or carbon are robustly detected in an absorption system, the column density ratio can be calculated directly. We take the column density measurements of saturated systems at face value, although they have large associated uncertainties. 12 systems have both C II and C IV detected and are classified as ‘carbon both’ in the analysis, and 14 systems have both Si II and Si IV detected and are classified as ‘silicon both’. For systems in which only one ion is present or either ion is flagged as an upper limit in Davies et al.

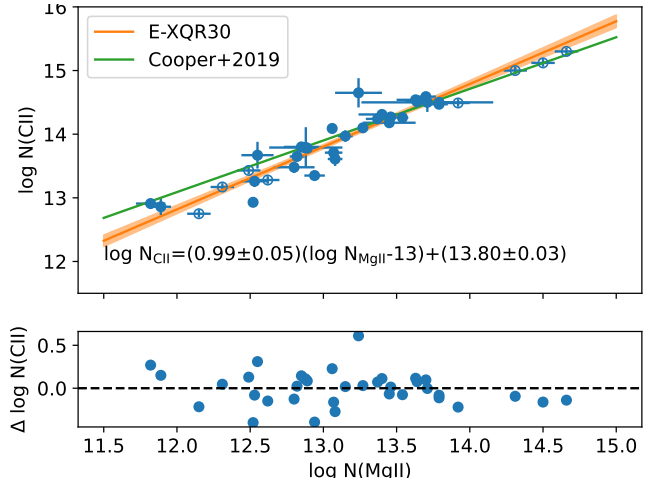


Figure 1. The column densities of C II and Mg II for 29 absorption systems at $5.3 < z < 6.4$ from the E-XQR-30 metal absorber catalogue. Measurements for systems with saturated absorption or evidence of partial covering are plotted as open markers. The orange line represents the linear fit to the E-XQR-30 data and the green line indicates the fit from Cooper et al. (2019). The bottom panel shows the residual scatter of the C II column densities from the linear regression model.

(2023a), we calculate a limit on the column density ratio based on the noise in the spectrum, as described in Section 2.4. 9 systems are only detected in C II and classified as C II-only, resulting in a lower limit on the column density ratio. 34 systems have only C IV detected and are similarly classified as C IV-only, resulting in an upper limit on the column density ratio. The same applies to the silicon systems. The final absorber sample is summarised in Table 2.

2.3 Magnesium Measurements

C II 1334 Å cannot be detected at $z < 5.17$ in the E-XQR-30 sample due to overlap with the saturated Ly α forest. To quantify the $N_{\text{CII}}/N_{\text{CIV}}$ ratio at lower redshifts, we use Mg II 2796 Å as a proxy for C II. Mg II has an ionization potential of 7.6 eV, close to that of C II, and Cooper et al. (2019) demonstrated that there is a linear correlation between N_{CII} and N_{MgII} . We verify this correlation with the deeper E-XQR-30 dataset using the 37 systems where both Mg II and C II are detected, spanning $5.3 \leq z \leq 6.4$. We perform a linear fit using the orthogonal distance regression (ODR) method from the `scipy.odr` PYTHON package, accounting for the errors on the measurements. The C II and Mg II column density measurements are shown in Figure 1, with our linear fit plotted in orange and the best-fit from Cooper et al. (2019) shown in green. Both correlations are consistent given the 1 sigma errors. Our best-fit relation between $\log(N_{\text{MgII}})$ and $\log(N_{\text{CII}})$ is given by the following equation:

$$\log(N_{\text{CII}}) = (0.99 \pm 0.05) [\log(N_{\text{MgII}}) - 13] + (13.80 \pm 0.03) \quad (1)$$

The slope is consistent with unity, suggesting that the ratio between the fraction of carbon in C II and the fraction of magnesium in Mg II does not vary significantly with column density over $\log(N_{\text{MgII}}/\text{cm}^{-2}) = 12.0 – 14.0$. The $\log(N_{\text{CII}}/N_{\text{MgII}})$ ratio is constant at ~ 0.8 , very similar to the relative [C/Mg] abundance measured in the solar photosphere of 0.83 dex (Asplund et al. 2009). We note that the 50% completeness limit for detection of Mg II is $\log(N_{\text{MgII}}/\text{cm}^{-2}) \approx 12.3$, which based on Equation 1 corresponds to

Dataset Redshift	n (E-XQR-30)			n (Cooper et al. 2019)			n (Boksenberg et al. 2015) 2 < z < 4.4
	4.3 < z < 5.17	5.17 < z < 5.7	z > 5.7	4.3 < z < 5.17	5.17 < z < 5.7	z > 5.7	
C II + C IV	N/A	3	9	N/A	0	6	22
C II, no C IV	N/A	4	5	N/A	2	10	N/A
C IV, no C II	N/A	15	20	N/A	5	4	39
Mg II + C IV	52	17	6	1	6	0	N/A
Mg II, no C IV	5	11	6	3	4	1	N/A
C IV, no Mg II	264	52	13	2	6	0	N/A
Si II + Si IV	2	6	6	0	4	4	4
Si II, no Si IV	0	1	6	1	5	12	N/A
Si IV, no Si II	15	41	15	1	7	2	10

Table 2. The number of absorption systems, denoted as n , in the E-XQR-30, [Cooper et al. \(2019\)](#) and [Boksenberg & Sargent \(2015\)](#) samples that have one or both of C II and C IV, Mg II and C IV, and Si II and Si IV. ‘C IV, no C II’ refers to systems with detections of C IV and not C II within the C II redshift range. These systems overlap with ‘C IV, no Mg II’ which refers to detections of C IV with no Mg II within the Mg II redshift range. Mg II is not accessible for some C II systems at $z > 5.7$ due to skyline contamination. ‘N/A’ indicates redshift ranges where one or both of the relevant ions are detectable or combinations of ions not probed by the dataset.

$\log(N_{\text{CII}}/\text{cm}^{-2}) \simeq 13.1$; very close to the measured 50% completeness limit for C II of $\log(N_{\text{CII}}/\text{cm}^{-2}) \simeq 13.0$ ([Davies et al. 2023a](#)). This suggests that using Mg II as a proxy for C II does not significantly change the column density sensitivity for detection of low-ionization absorbers in our sample.

We use Equation 1 to obtain Mg II column density measurements or upper limits for 426 systems. Of these, 61 have solid Mg II detections but no coverage of C II, allowing us to use Equation 1 to infer N_{CII} . We note that we find consistent results for the fraction of systems with low ionization, high ionization, and mixed absorption when using C II or Mg II (see Section 3.1).

2.4 Column Density Limits

We calculate the 3σ upper limit on the column density of each undetected line by summing the errors in quadrature over the relevant wavelength region to determine the maximum absorption equivalent width and then converting this equivalent width to a column density assuming it lies on the linear part of the curve of growth.

For each undetected feature, we consider that absorption may be present between $\lambda_{\text{obs}} - \Delta\lambda/2$ and $\lambda_{\text{obs}} + \Delta\lambda/2$. Within a single absorption system, different species can have different velocities and widths (see [Davies et al. 2023a](#)). To ensure that we cover all wavelengths where absorption could be present, we calculate $\Delta\lambda$ as the wavelength interval corresponding to a velocity range of 200 km/s. The vast majority of metal absorbers in E-XQR-30 have a 90% velocity width (v_{90}) less than 200 km/s, and therefore this provides a conservatively high estimate for the equivalent width upper limit. The 1σ upper limit on the equivalent width of undetected absorption is computed by summing the equivalent width error in quadrature over this wavelength range assuming uncorrelated noise:

$$dEW = \sqrt{\int_{\lambda_{\text{obs}} - \Delta\lambda/2}^{\lambda_{\text{obs}} + \Delta\lambda/2} \left(\frac{\text{error}(\lambda)}{\text{continuum}(\lambda)} \right)^2 d\lambda} \quad (2)$$

Here, $d\lambda$ is the width of each spectral channel in angstroms. The observed equivalent width limit is converted to rest frame by dividing by $(1+z)$. To convert the rest frame EW limit to a column density limit, we use a modified version of the equation provided in section 4.2 of [Cackett et al. \(2008\)](#), which assumes that the absorption lies

on the linear part of the curve of growth:

$$dN(\text{cm}^{-2}) = \frac{dEW_{\text{rest}}(\text{\AA})}{8.85 \times 10^{-21} \times \lambda_{\text{rest}}(\text{\AA})^2 \times f} \quad (3)$$

Here, f denotes the oscillator strength. To obtain a 3σ upper limit on the column density, we multiply the result obtained by 3.

2.5 Literature Comparison Samples

We compare our E-XQR-30 measurements with the results of [Cooper et al. \(2019\)](#). They identified 69 systems with Mg II, C IV and/or Fe II absorption at $5 < z < 6.8$ and then fit for C II, Si II, and Si IV in the identified systems. This method, similar to that used by E-XQR-30, allows for the recovery of low ionization, high ionization, and mixed ionization systems. We use the data tables from [Cooper et al. \(2019\)](#) to calculate the $\log(N_{\text{CII}}/N_{\text{CIV}})$ and $\log(N_{\text{SiII}}/N_{\text{SiIV}})$ ratios as well as the fraction of low ionization, high ionization, and mixed ionization systems.

To extend our analysis to lower redshifts, we also utilise measurements from [Boksenberg & Sargent \(2015\)](#) which characterises absorption systems at redshifts $2 < z < 4.4$. Their paper presents comprehensive information on the column densities of several kinematic components in each absorption system, where systems are manually defined to encompass all velocity components within well-defined clumps of absorption with widths ranging up to a few hundred km s⁻¹. For consistency with the E-XQR-30 and [Cooper et al. \(2019\)](#) measurements, we sum the column densities of individual components to determine the total column density for each species in each absorption system. We only select systems for which all components have both N_{CIV} and N_{CII} measurements or limits and are not impacted by blending or other observational artifacts. When all components have robustly measured column densities, we directly sum the column densities and associated variance. If any component has a column density upper limit, that component is treated as having zero column density and the limit value is added (in quadrature) to the upper error on the column density of the system. This causes the column density measurements to have asymmetric errors. We note that only absorbers with C IV detections were initially included in the [Boksenberg & Sargent \(2015\)](#) sample. C II-only systems are not considered, and therefore this sample cannot be used to compute the fraction of low-ionization, high-ionization and mixed absorbers at $2 < z < 4.4$. For this reason, the [Boksenberg & Sargent \(2015\)](#)

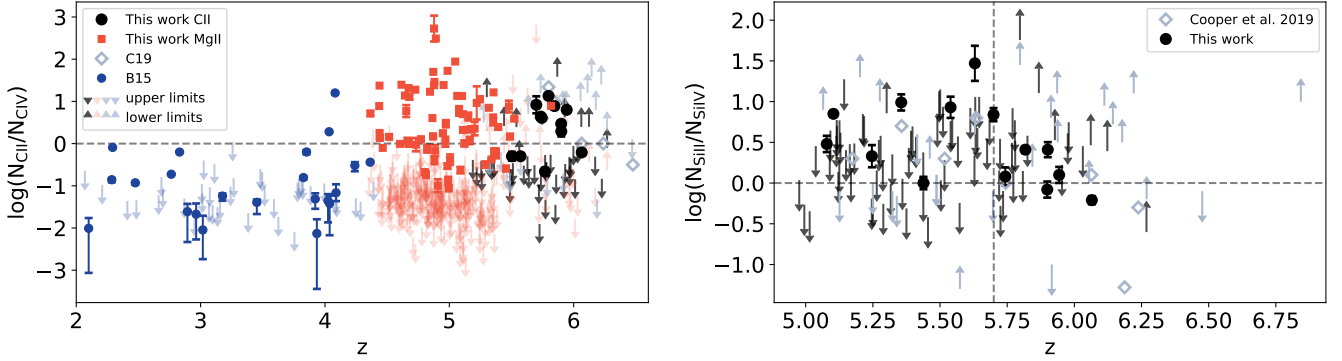


Figure 2. Evolution of $\log(N_{\text{CII}}/N_{\text{CIV}})$ (left) and $\log(N_{\text{SIII}}/N_{\text{SIV}})$ (right) as a function of redshift with upper and lower limit values denoted by downward and upward arrows respectively. Our E-XQR-30 $\log(N_{\text{CII}}/N_{\text{CIV}})$ and $\log(N_{\text{SIII}}/N_{\text{SIV}})$ measurements are shown in black, and measurements where Mg II is used as a proxy for C II are shown in orange. The [Cooper et al. \(2019\)](#) measurements (C19) are shown in grey and the [Boksenberg & Sargent \(2015\)](#) (B15) measurements are shown in blue. The dashed horizontal lines mark the location for equal quantities of singly and triply ionized metals.

sample is only used to examine how the $\log(N_{\text{CII}}/N_{\text{CIV}})$ ratio evolves towards lower redshifts. When quantifying the line ratio evolution we account for differences between the column density sensitivities of the E-XQR-30 and [Boksenberg & Sargent \(2015\)](#) datasets, as described in Section 3.2.

The properties of all datasets used in this analysis are summarized in Table 2.

3 RESULTS

The left-hand panel of Figure 2 shows the evolution of $\log(N_{\text{CII}}/N_{\text{CIV}})$ as a function redshift. Black points are E-XQR-30 measurements for systems where C II is covered, red points are E-XQR-30 measurements using Mg II as a proxy for C II , grey points show data from [Cooper et al. \(2019\)](#) and blue points show data from [Boksenberg & Sargent \(2015\)](#). This figure does not display Mg II measurements for systems where C II is accessible. Measurements for mixed systems are denoted by solid symbols with error bars, and arrows represent upper (lower) limits for systems with only high-ionization (low-ionization) absorption. The plot appears to reveal a decrease in $\log(N_{\text{CII}}/N_{\text{CIV}})$ towards lower redshifts, primarily driven by the disappearance of systems with large $\log(N_{\text{CII}}/N_{\text{CIV}})$ ratios at $z \lesssim 4$. We emphasize that the [Boksenberg & Sargent \(2015\)](#) sample does not include C II -only low-ionisation absorbers and therefore it is not possible to probe systems with lower limits on $\log(N_{\text{CII}}/N_{\text{CIV}})$ at $z < 4.3$. The right-hand panel of Figure 2 shows the evolution of $\log(N_{\text{SIII}}/N_{\text{SIV}})$ over the redshift range covered by the E-XQR-30 and [Cooper et al. \(2019\)](#) samples. There is no clear evidence for any variation in ionization properties with redshift, perhaps due to the much shorter redshift interval probed.

We quantify the evolution in the ionization states of the metal absorbers using two methods. We first compute the fraction of low-ionization, high-ionization and mixed absorbers in 3 redshift bins (Section 3.1), and then perform linear regression to quantify the redshift evolution of the $N_{\text{CII}}/N_{\text{CIV}}$ ratio for mixed absorbers where both species are detected (Section 3.2).

3.1 Fraction of Low-Ionization, High-Ionization and Mixed Absorbers

For each combination of ions ($\text{C II} + \text{C IV}$, $\text{Mg II} + \text{C IV}$, $\text{Si II} + \text{Si IV}$), we compute the number of absorption systems with only low

ionization, only high ionization, or both ions detected, in 3 redshift bins: $z < 5.17$, $5.17 < z < 5.7$ and $z > 5.7$ (Table 2). The $z = 5.17$ partition represents the lower boundary for C II detection while $z = 5.7$ is the redshift of the reported transition between low-ionization-dominated and high-ionization-dominated absorbers in [Cooper et al. \(2019\)](#). The Mg II-C IV statistics include systems where both C II and Mg II are accessible. We then compute the fraction of ions in each category as a function of redshift, shown in Figure 3. The 1σ errors on the fractions are computed assuming Poisson statistics, using Equations 9 and 12 from [Gehrels \(1986\)](#) with $s = 1$ and $\beta = 0$, appropriate for a 1σ confidence interval. These equations are more accurate than the typical $\text{sqrt}(N)$ approximation for small samples.

The left-hand panel of Figure 3 reveals a strong evolution in the ionization state of carbon and magnesium absorbers over redshift. At $5.7 < z < 6.3$, 52% of absorbers have C IV but no Mg II , 24% have both Mg II and C IV and 24% have Mg II but no C IV , whilst at $4.3 < z < 5.17$, 82% of absorbers have C IV but no Mg II , 16% have both Mg II and C IV and just 2% have Mg II but no C IV . Silicon absorbers, shown in the right panel, show similar trends to the carbon absorbers at $z > 5.17$ where both can be measured. The observed decrease in the incidence of low-ionization absorbers and corresponding increase in high-ionization absorbers towards lower redshifts is qualitatively consistent with previous findings (e.g. [Becker et al. 2019](#); [D’Odorico et al. 2022](#); [Davies et al. 2023b](#); [Sebastian et al. 2024](#)).

Interestingly, our observed evolution is much weaker than what was reported in [Cooper et al. \(2019\)](#). They found that 52% of carbon absorption systems at $z > 5.7$ only show low ionization absorption; a factor of 2 larger than the 24% reported in this study. This is likely driven by differences in the column density sensitivity of the datasets. The column density limit for the [Cooper et al. \(2019\)](#) FIRE spectra is $\log(N/\text{cm}^{-2}) \gtrsim 13.5$, compared to 50% completeness limits of $\log(N_{\text{CIV}}/\text{cm}^{-2}) = 13.2$ and $\log(N_{\text{CII}}/\text{cm}^{-2}) = 13.0$ for E-XQR-30. 81% of the C IV absorbers detected by E-XQR-30 lie below the 50% completeness limit in [Cooper et al. \(2019\)](#), and the 2–3 times deeper E-XQR-30 observations show that C IV absorbers heavily dominate the absorber population by number density at all redshifts (Figure 3 left). To investigate the impact of sensitivity on the measured absorber fractions, we re-calculated the absorber fractions only including detections above the detection limit of the FIRE spectra. [Cooper et al. \(2019\)](#) quote an approximate detection limit of $\log(N_{\text{CII}}/\text{cm}^{-2}) > 13.5$, which based on Equation 1 corresponds to

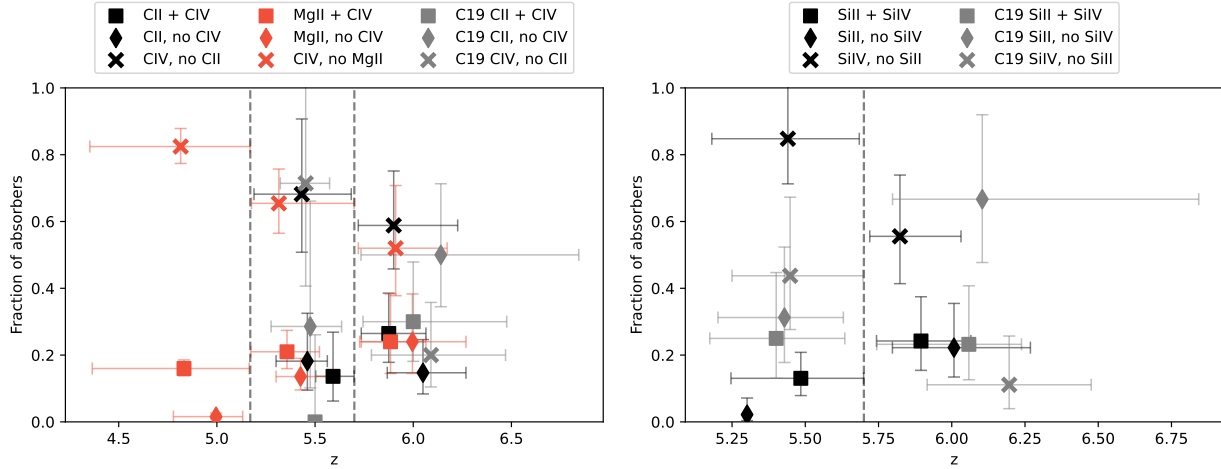


Figure 3. The fraction of absorbers detected in carbon/magnesium (left) and silicon (right) with low-ionization, high-ionization or mixed absorption, split into redshift bins $4.34 < z < 5.17$ (carbon only), $5.17 < z < 5.7$ and $5.7 < z < 6.5$. The color-coding of the samples is the same as in Figure 2. Horizontal error bars show the span of redshifts occupied by absorbers and vertical error bars show the 1σ error on the fraction measurements. Some points have been offset by up to 0.02 on either axis for clarity.

$\log(N_{\text{MgII}}/\text{cm}^{-2}) \gtrsim 12.7$. Based on results from E-XQR-30 (Davies et al. 2023a), we assume a comparable detection limit in CIV, i.e. $\log(N_{\text{CIV}}/\text{cm}^{-2}) > 13.5$. We found that imposing this cut increases the fraction of Mg II-only systems at $z > 5.7$ by more than a factor of 2, from 24% to 56% such that these absorbers dominate the population at that redshift, consistent with the Cooper et al. (2019) results. The fraction of Mg II-only systems at $5.17 < z < 5.7$ also increases from 2% to 25%, but C IV-only absorbers are still dominant, accounting for 45% of systems at this redshift. These results suggest that the balance between high-ionization and low-ionization gas may differ for strong and weak absorbers.

Nevertheless, our results support the existence of a significant population of low-ionization-only absorbers at $z > 5.7$. Such systems are not expected based on our canonical picture of the low redshift CGM whereby dense, low-ionization clouds with a small volume filling factor are surrounded by higher ionization clouds with a larger covering fraction. In this scenario, we would expect metal absorber samples to be comprised primarily of high-ionization and mixed absorbers, with very few systems displaying only low-ionization absorption.

We further explore the characteristics of the different absorber populations by comparing their kinematics quantified using v_{90} which is the velocity interval enclosing 90 per cent of the optical depth for a single transition of a given absorption species. Combining all redshift ranges, C IV-only absorbers have an average v_{90} of $98 \pm 56 \text{ km s}^{-1}$ while C II-only and Mg II-only absorbers have a lower average v_{90} of $68 \pm 27 \text{ km s}^{-1}$. This is consistent with the overall statistics from the E-XQR-30 metal absorber catalog which show that individual components of high ionization absorbers generally have larger linewidths than components of low ionization absorbers (Davies et al. 2023a). Our findings are also consistent with many previous works suggesting that high ionization absorbers on average are expected to arise from warmer and more turbulent material (e.g. Wolfe et al. 1993; Rauch et al. 1996; Lehner et al. 2014; Muzahid 2014; Fox et al. 2015; Pradeep et al. 2020). Interestingly, mixed ionization systems have the highest average v_{90} of $157 \pm 79 \text{ km s}^{-1}$ for C IV absorption and $108 \pm 67 \text{ km s}^{-1}$ for Mg II absorption, suggesting they trace more complex multiphase systems, consistent with the findings of Codoreanu et al. (2018). There is weak evidence for an increase in the average $v_{90}(\text{C IV})$ of mixed absorbers towards lower redshift, from $125 \pm 71 \text{ km s}^{-1}$ at $z > 5.17$ to $175 \pm 80 \text{ km s}^{-1}$ at $4.3 < z < 5.17$.

This is primarily driven by a slight increase in the average number of kinematic components per absorption system from 1.3 to 1.7, with no significant change in the turbulent b parameter of individual components.

Cooper et al. (2019) suggest that the detection of a significant population of C II-only absorbers at $z > 5.7$ may indicate that the CGM at this redshift has a lower ionization state (see also Becker et al. 2019 and/or is significantly more metal-poor than the CGM at $z \sim 3$. These possibilities will be discussed further in Section 4.

3.2 The $\log(N_{\text{CII}}/N_{\text{CIV}})$ Column Density Ratio

3.2.1 Redshift Evolution

We quantify the evolution of $\log(N_{\text{CII}}/N_{\text{CIV}})$ as a function of redshift by fitting a linear relation. We only use mixed systems when calculating the redshift evolution of the $N_{\text{CII}}/N_{\text{CIV}}$ ratio because the low and high ionization systems likely trace predominately single-phase gas and therefore the lower and upper limits on the $N_{\text{CII}}/N_{\text{CIV}}$ ratios measured for these systems mostly reflect the measurement uncertainties rather than the intrinsic properties of the absorption systems. In addition, we only consider systems with column densities above the 50% completeness limit of the E-XQR-30 sample ($\log(N_{\text{CII}}) > 13.0$, $\log(N_{\text{CIV}}) > 13.2$) to prevent biases that may arise due to comparing systems with different column densities at different redshifts. The background markers in Figure 4 show the measurements included in this analysis.

The vast majority of our $\log(N_{\text{CII}}/N_{\text{CIV}})$ measurements are at $4.3 \lesssim z \lesssim 5.17$, so to prevent the best-fit being solely driven by this redshift interval, we bin the data and compute the median $\log(N_{\text{CII}}/N_{\text{CIV}})$ ratio and the associated error ($1.253\sigma/\sqrt{N}$) in each redshift bin. We try bin sizes of $0.2 < \Delta(z) < 1.0$ and select a bin size of $\Delta(z) = 0.6$ which produces the best compromise between number of bins and number of objects per bin. Our median measurements are shown by the green markers and the best fit line is over-plotted in green with the shaded region indicating the $\pm 1\sigma$ error interval.

For the fiducial bin size of $\Delta(z) = 0.6$, we measure a slope of 0.33 ± 0.08 . Our results indicate that the $N_{\text{CII}}/N_{\text{CIV}}$ ratio declines by a factor of ~ 20 between $z \sim 6$ and $z \sim 2$, with a significance of $\sim 4\sigma$. We test the impact of the chosen bin size on this result and find that for

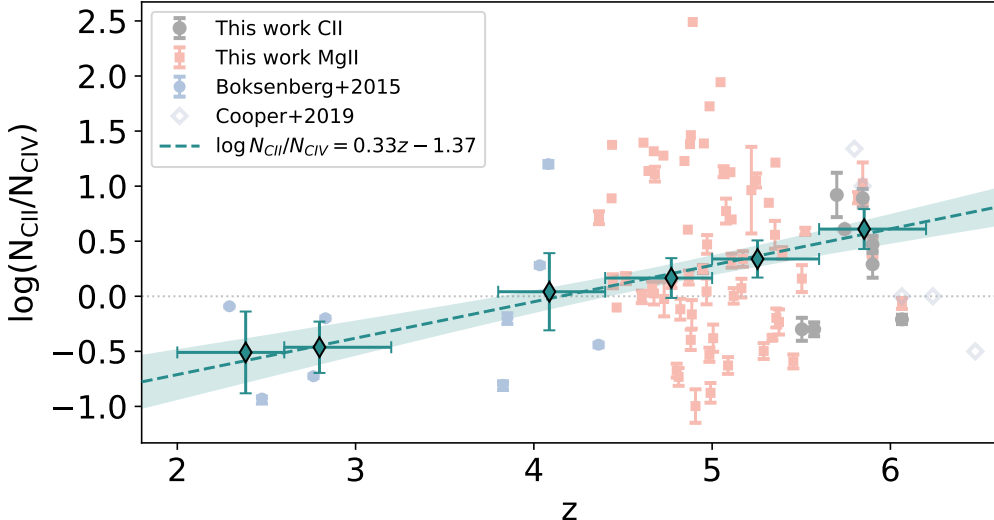


Figure 4. Measurements of the $\log(N_{\text{CII}}/N_{\text{CIV}})$ ratio for mixed absorption systems with column densities above the 50% completeness limit of the E-XQR-30 catalog ($\log(N_{\text{CII}}) > 13.0$, $\log(N_{\text{CIV}}) > 13.2$ (background)). Green solid markers show medians and associated error ($1.253\sigma/\sqrt{N}$) in bins of redshift. The linear fit to these medians reveals a clear decline in $\log(N_{\text{CII}}/N_{\text{CIV}})$ towards lower redshift.

bin sizes of $0.2 < \Delta(z) < 1.0$, the slope varies from $0.26 - 0.34$, within the margin of error of the original estimate. There is some evidence that the $N_{\text{CII}}/N_{\text{CIV}}$ ratio decreases slightly over the E-XQR-30 redshift range from $z \sim 6.3$ to $z \sim 4.3$, primarily because most of mixed absorbers at $z \gtrsim 5.5$ are dominated by high ionization absorption with $\log(N_{\text{CII}}/N_{\text{CIV}}) > 0$. However, this evolution is not statistically significant due to the small number of systems in the highest redshift bin and the large intrinsic scatter in the $z \approx 5$ measurements.

The decrease in the average $N_{\text{CII}}/N_{\text{CIV}}$ ratio of mixed absorbers towards lower redshift supports the conclusions from the fraction analysis that the average ionization state of metal absorbers increases over cosmic time.

3.2.2 Correlation with ion column densities

Figure 5 examines how the $\log(N_{\text{CII}}/N_{\text{CIV}})$ ratio correlates with the column densities of the individual ions: $\log(N_{\text{CII}})$ (top left) and $\log(N_{\text{CIV}})$ (top right). The results are striking: the column density ratio shows a strong positive correlation with $\log(N_{\text{CII}})$ but is virtually independent of $\log(N_{\text{CIV}})$.

To investigate whether the redshift evolution in $\log(N_{\text{CII}}/N_{\text{CIV}})$ is driven by a decrease in the typical $\log(N_{\text{CII}})$ towards lower redshifts, we calculated the expected $\log(N_{\text{CII}}/N_{\text{CIV}})$ of each absorber based on its measured $\log(N_{\text{CII}})$, subtracted this from the measured ratio, and then plotted the residuals as a function of redshift. The results are shown in the bottom left panel of Figure 5. Accounting for the trend with $\log(N_{\text{CII}})$ significantly reduces the scatter at fixed redshift compared to Figure 4 but does not significantly change the slope of the redshift evolution. If we instead compute the residuals from the $\log(N_{\text{CIV}})$ correlation, the ratios remain essentially unchanged (see bottom right panel of Figure 5), as expected given that the $\log(N_{\text{CIV}})$ trend is relatively weak.

Our results indicate that the redshift evolution in the $\log(N_{\text{CII}}/N_{\text{CIV}})$ ratio is not driven by differences in the typical column densities of absorbers probed at each redshift. The top panels show that we probe similar column densities at all redshifts, which is a direct consequence of the fact that we remove systems from the Boksenberg & Sargent (2015) sample that fall below the detection

limit of E-XQR-30. Furthermore, the redshift trends remain essentially unchanged even after accounting for correlations with column density.

4 DISCUSSION

The unprecedented depth and sample size of the E-XQR-30 catalog have enabled us to robustly demonstrate that the ionization state of circumgalactic gas evolves significantly in the early Universe. The fraction of low-ionization absorbers declines significantly over a period of less than 400 Myr, from 24% at $z \sim 6$ to just 2% at $z \sim 4.7$. Furthermore, the typical $N_{\text{CII}}/N_{\text{CIV}}$ ratio of mixed absorbers declines by a factor of 20 over the 2 Gyr from $z \sim 5.9$ to $z \sim 2.3$.

We used the CLOUDY photoionization code (Ferland et al. 2017) to investigate the physical mechanisms driving the decline in the $N_{\text{CII}}/N_{\text{CIV}}$ ratio towards lower redshifts. We run models of CGM clouds with solar-scaled abundances (Grevesse et al. 2010) illuminated using the Haardt & Madau (2012, hereafter HM12) UV background model. Following the approach of Cooper et al. (2019), we explore the impact of varying hydrogen volume density and metallicity at fixed redshift ($z = 4, 5, 6$) and N_{HI} (10^{15} cm^{-2} , 10^{17} cm^{-2} and 10^{19} cm^{-2}), covering column densities representative of environments ranging from the densest regions of the intergalactic medium to the neutral circumgalactic medium (e.g. Péroux & Howk 2020). We note that fixing the H I column density makes the results relatively insensitive to the choice of UVB model: in Appendix A we show that consistent results are obtained using the Puchwein et al. (2019) and Faucher-Giguère (2020) UV background models which are in better agreement with estimates of the H I photoionization rate at $z=5-6$. We caution though that these photoionization models are quite simple, as C II and C IV absorbers likely trace gas at different column densities and metallicities.

The photoionization model results are shown in Figure 6. The black solid (dashed) lines delineate the 50% completeness limit for detection of C II ($N_{\text{CII}} = 10^{13} \text{ cm}^{-2}$) and C IV ($N_{\text{CIV}} = 10^{13.2} \text{ cm}^{-2}$) in the E-XQR-30 dataset. The column densities of both species correlate strongly with metallicity, whilst the C IV column density also

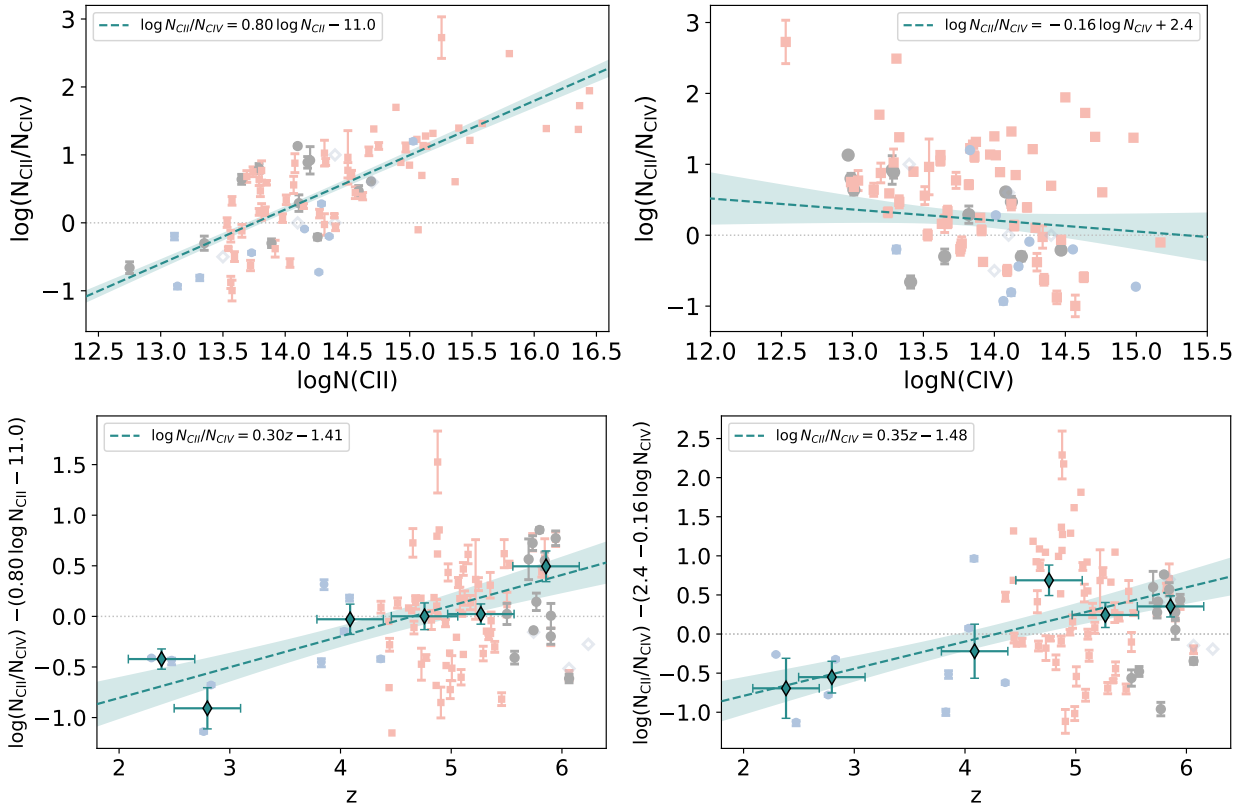


Figure 5. Top: $\log(N_{\text{CII}}/N_{\text{CIV}})$ correlates strongly with $\log(N_{\text{CII}})$ (left) but shows little dependence on $\log(N_{\text{CIV}})$ (right). Bottom: accounting for the correlations with $\log(N_{\text{CII}})$ (left) or $\log(N_{\text{CIV}})$ (right) reduces the scatter in $\log(N_{\text{CII}}/N_{\text{CIV}})$ at fixed redshift but does not significantly impact the observed redshift evolution. Plot symbols are the same as in Figure 4.

decreases towards higher hydrogen volume density where carbon is primarily found in lower ionization states (see also Davies et al. 2023a). In contrast, the C II column density is relatively independent of hydrogen volume density, as it is more sensitive to the ionization parameter. Whether a C II-only absorber, C IV-only absorber, C II + C IV absorber or no detection would occur at a given hydrogen volume density H_1 column density depends on the metallicity and probed by the absorbers. It is likely that not all of the parameter space shown here may not correspond to realistic properties of true $z = 4 - 6$ absorbers, e.g., it is not expected to see C IV-only systems with $N_{\text{HI}} = 10^{19} \text{ cm}^2$. These models do, however, demonstrate that a wide range of values for $N_{\text{CII}}/N_{\text{CIV}}$ are possible, depending on the physical properties of the absorbers. This is in good agreement with the spread of values measured in Figure 2, especially when considering the upper and lower limits.

4.1 Impact of metallicity

The first important result demonstrated by Figure 6 is that our ability to detect C II and C IV is strongly metallicity-dependent. Focusing on the upper middle panel, at fixed column density ratio $\log(N_{\text{CII}}/N_{\text{CIV}}) = -1$, an absorber might be detected in both C II and C IV, or C IV only, or neither depending on its metallicity. The impact of metallicity on the detectability of C II and C IV is especially relevant at high redshifts because the gas giving rise to these lines is likely not co-spatial and the metallicity may differ significantly between C II-hosting and C IV-hosting regions (e.g. Cooper et al. 2019). The denser C II-hosting regions are likely to reside closer to galax-

ies and therefore become enriched with metals earlier than the more diffuse C IV-hosting regions further out in the halo. Star-forming galaxies during the epoch of reionization are embedded in massive reservoirs of C II-emitting cold gas (e.g. Fujimoto et al. 2019; Ginolfi et al. 2020; Bischetti et al. 2024, 2025) which simulations predict are likely enriched by feedback processes (e.g. Vito et al. 2022; Pizzati et al. 2023). Davies et al. (2023b) showed that the rapid evolution in the C IV cosmic mass density between $z \sim 6.3$ and $z \sim 4.3$ could be explained by chemical enrichment if the delay time for outflows enrich diffuse gas in the outer halo is on the order of 100 – 400 Myr. This is also consistent with the measured outflow velocities and impact parameters of C IV absorbers at this redshift. The upper right panel of Figure 6 suggests that, at $z \sim 6$, diffuse, low metallicity gas in the halo could remain mostly undetected, whilst denser, more enriched gas could be detected as C II-only or C II + C IV absorption. At $z \sim 4$, the predicted detection statistics are significantly different, favouring C II+C IV and C IV-only absorption and disfavouring C II-only absorption. This predicted shift is consistent with the ionization fraction trends observed in Figure 3. The diversity in observed C II-only, C IV-only and mixed systems at fixed redshift could be explained if the E-XQR-30 absorbers show a spread in metallicity as wide as what is observed at $z \sim 3$ (e.g. Lehner et al. 2022) and there is also some variation in the gas density and N_{HI} probed by the absorbers.

4.2 Impact of H_1 column density

Comparing the grids in the top, middle and bottom rows of Figure 6, it is clear that the observed absorber statistics are strongly depen-

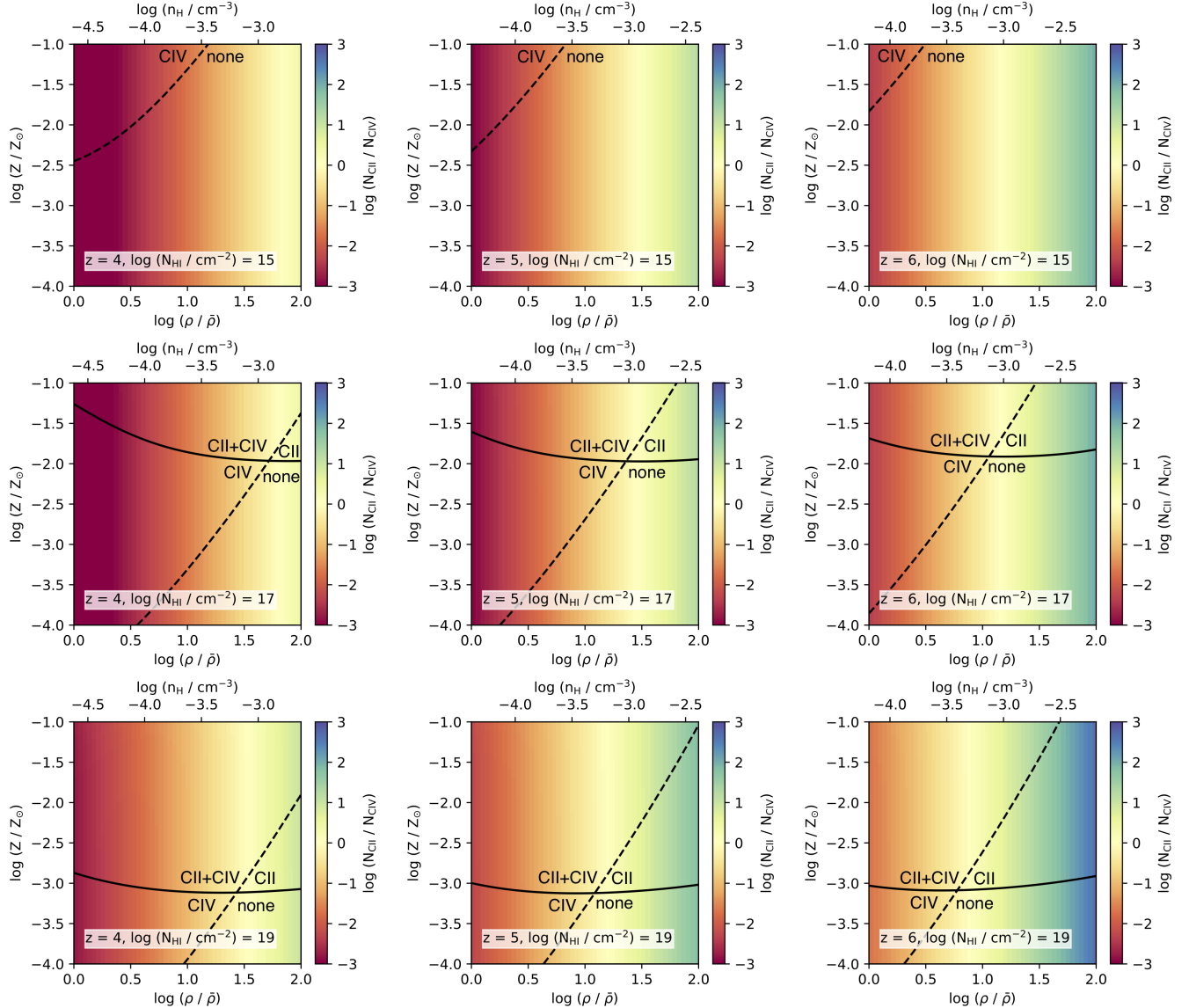


Figure 6. Photoionization models of $\log(N_{\text{CII}}/N_{\text{CIV}})$ as a function of metallicity (y-axis), hydrogen column density (upper x-axis), and density normalized to the cosmic mean at the relevant redshift (lower x-axis) for gas clouds at fixed neutral hydrogen column density (rows) and redshift (columns), illuminated by a Haardt & Madau (2012) UV background. The range of density in units of the cosmic mean is the same in all panels, while the corresponding range of proper hydrogen number density changes with redshift. The black solid (dashed) lines mark the column density of the 50% completeness limit for C II (C IV) absorbers in the E-XQR-30 dataset, corresponding to $N_{\text{CII}} = 10^{13} \text{ cm}^{-2}$ and $N_{\text{CIV}} = 10^{13.2} \text{ cm}^{-2}$. These different quadrants indicate the detectability of C II and C IV absorption: C II-only, no detection, C IV-only, and C II + C IV. For the lowest H I column density considered here, $N_{\text{HI}} = 10^{15} \text{ cm}^{-2}$, C II would not be detectable for gas in the metallicity and density range probed by these models.

dent on H I column density. For $N_{\text{HI}} = 10^{19} \text{ cm}^{-2}$, C II-only and C II + C IV absorbers are expected to dominate at most metallicities, whilst for $N_{\text{HI}} = 10^{17} \text{ cm}^{-2}$, C IV-only absorbers become much more prominent at low metallicities and densities. At $N_{\text{HI}} = 10^{15} \text{ cm}^{-2}$, only C IV systems are expected to be detectable. If the typical H I column densities of metal absorption systems decrease towards lower redshifts (as the UV background evolves), the fraction of low-ionization, high-ionization and mixed absorbers would change in a qualitatively similar manner to what is observed in E-XQR-30.

Islands of neutral gas act as effective sinks for ionizing photons, and as these neutral islands disappear, the mean free path of ionizing photons increases significantly (Becker et al. 2021; Gaikwad et al. 2023; Zhu et al. 2023; Satyavolu et al. 2024). This is expected to drive

a rapid increase in the strength of the UV background (Lewis et al. 2022) between $z \sim 6$ and $z \sim 5$, consistent with observations showing that the H I photoionization rate rises sharply over this redshift range (Calverley et al. 2011; Gaikwad et al. 2023; Davies et al. 2024).

The increase in the H I photoionization rate directly impacts the density at which gas begins to self shield and is therefore expected to induce rapid evolution in the typical column density of H I absorbers (Schaye 2001). Assuming the evolution in H I photoionization rate measured by Gaikwad et al. (2023), the threshold self-shielding density would increase by a factor of approximately 2.5 between $z \sim 6$ and $z \sim 5$, meaning that the circumgalactic medium will be self-shielded to smaller and smaller radii as the amplitude of the UVB increases (Sadoun et al. 2017).

The shape of the H I column density distribution function is difficult to measure directly near the EoR due to the saturation of the Ly α forest (Fan et al. 2006). The highest redshift measurement to date is at $z \sim 5$ (Crighton et al. 2019), which still shows a smooth evolution when compared to lower redshift data. However, there is some evidence that the H I column density distribution should evolve more rapidly towards higher redshifts. The incidence of Lyman-limit systems ($N_{\text{H I}} = 10^{17.2} - 10^{19} \text{ cm}^{-2}$) is observed to increase with redshift towards $z \sim 6$ (Songaila & Cowie 2010), whilst the incidence of DLAs ($N_{\text{H I}} > 10^{20.3} \text{ cm}^{-2}$) appears to peak at $z \sim 4$ and decrease significantly towards higher redshifts (Oyarzún et al. 2025). The fraction of galaxies showing strong Ly α emission decreases towards high redshift, with some evolution already seen between redshifts 5 and 6 (Tang et al. 2024). If the typical H I column density of a metal absorber host evolves from something like a Lyman-limit system at lower redshifts, to something closer to a sub-DLA ($N_{\text{H I}} = 10^{19} - 10^{20.3} \text{ cm}^{-2}$) at higher redshifts, this may explain the change in the relative fractions of low-ionization, high-ionization and mixed absorbers with redshift. In this scenario, the metal absorbers would be in good agreement with other indirect probes of the evolution of H I absorbers in ionized regions towards the end of reionization.

The majority of the scatter in the observed $\log(N_{\text{CII}}/N_{\text{CIV}})$ ratios can likely be explained by local fluctuations in the gas density, ionization parameter and metallicity. Prior to the end of reionization, spatial fluctuations in the UV background cause large-scale variations in the mean flux of the Ly α forest (Bosman et al. 2022) and may also enhance the scatter in $\log(N_{\text{CII}}/N_{\text{CIV}})$ above $z \simeq 5$. However, there are too few measurements at $z < 4.5$ to enable a robust measurement of intrinsic scatter as a function of redshift.

5 CONCLUSIONS

We have used a sample of 488 metal absorption systems at $4.3 \leq z \leq 6.3$ from the E-XQR-30 metal absorber catalog combined with 75 absorption systems at $2 \leq z \leq 4$ from Boksenberg & Sargent (2015) to investigate the evolution in the ionization properties of circumgalactic gas from the epoch of reionization to cosmic noon. Our results are based on analysis of the singly and triply ionized ions of carbon (C II and C IV) and silicon (Si II and Si IV). We also use Mg II as a proxy for C II to enable us to extend the analysis to $z < 5.17$ where C II falls in the Ly α forest.

Using 3 pairs of ions (C II + C IV, Mg II + C IV, Si II + Si IV), we classify absorption systems as low-ionization only, high-ionization only, or mixed ionization and investigate how the fraction of absorbers in each category evolves with redshift. For mixed absorbers where both ions are robustly detected, we compute the column density ratios $N_{\text{CII}}/N_{\text{CIV}}$ and $N_{\text{SiII}}/N_{\text{SiIV}}$ and investigate how these evolve over redshift. Our main conclusions are as follows:

(i) High-ionization systems dominate the absorber population by number density even at $z \sim 6$, contrary to previous findings. We recover a significant population of weak C IV absorbers that were likely undetected in previous large samples with lower spectral resolution and signal-to-noise.

(ii) The fraction of low-ionization systems (with detected Mg II but no C IV) declines significantly over a period of less than 400 Myr, from 24% at $z \sim 6$ to just 2% at $z \sim 4.7$. The fraction of high-ionization systems (with C IV but no Mg II) increases correspondingly from 52% at $z \sim 6$ to 82% at $z \sim 4.3$, with little change in the fraction of mixed systems.

(iii) The average $N_{\text{CII}}/N_{\text{CIV}}$ ratio of mixed absorbers declines by a factor of ~ 20 from $z \sim 6$ to $z \sim 2$, providing additional evidence for an increase in the ionization state of circumgalactic gas from the epoch of reionization to cosmic noon.

(iv) By running large grids of CLOUDY models, we show that at fixed n_{H} and N_{HI} , the detectability of C II and C IV is strongly dependent on metallicity. This is especially relevant at high redshifts because the denser C II-hosting regions reside closer to galaxies and likely become enriched with metals significantly earlier than the more diffuse C IV-hosting regions further out in the halo. The models suggest that at $z \sim 6$, diffuse, low metallicity halos gas could be detected at low C IV column density, whilst denser, more enriched gas could be detected as C II-only or C II + C IV absorption. At $z \sim 4$, this would transition to C II + C IV absorption closer to galaxies and stronger C IV-only absorption at larger distances. The observed diversity in C II-only, C IV-only and C II + C IV absorbers at fixed redshift can likely be explained by spreads in metallicity, gas volume density and H I column density.

(v) A decrease in the typical H I column density of metal absorbers towards lower redshifts, linked to the declining average cosmic mean density, would also lead to increasing dominance of high-ionization absorbers at lower redshifts. We hypothesize that the rapid evolution in the ionization states of metal absorbers between $z \sim 6$ and $z \sim 5$ could be driven by rapid changes in their H I column densities resulting from the disappearance of neutral islands and a corresponding increase in the mean free path of ionizing photons during the final stages of reionization. The timing of this transition is consistent with recent findings that reionization ends at $z=5.44 \pm 0.02$ (Qin et al. 2024).

Our results confirm that the ionization states of metal absorbers evolve significantly in the early Universe and highlight the complexities of disentangling the various factors contributing to this evolution.

ACKNOWLEDGEMENTS

We thank the referee for their thoughtful comments which improved the clarity of the manuscript. SR thanks Chris Blake for helpful discussions regarding the statistical analysis in this paper and acknowledges the Wurundjeri people of the Kulin nation who are the traditional custodians of the lands on which this research was conducted. This research was supported by the Australian Research Council Centre of Excellence for All Sky Astrophysics in 3 Dimensions (ASTRO 3D), through project number CE170100013. RLD is supported by the Australian Research Council through the Discovery Early Career Researcher Award (DECRA) Fellowship DE240100136 funded by the Australian Government. SEIB is supported by the Deutsche Forschungsgemeinschaft (DFG) under Emmy Noether grant number BO 5771/1-1. HC thanks the support by the Natural Sciences and Engineering Research Council of Canada (NSERC), funding reference #RGPIN-2025-04798 and #DGECR-2025-00136, and by the University of Alberta, Augustana Campus. VD and LW acknowledge financial support from the Bando Ricerca Fondamentale INAF 2022 Large Grant “XQR-30”. MH and GK acknowledge support by UKRI-STFC (grant reference ST/Y004191/1). GK is supported by the Department of Atomic Energy (Government of India) research project with Project Identification Number RTI 4002. Based on observations collected at the European Organisation for Astronomical Research in the Southern Hemisphere under ESO Programme IDs 0100.A-0625, 0101.B-0272, 0102.A-0154, 0102.A-0478, 084.A-0360(A), 084.A-0390(A), 084.A-0550(A), 085.A-0299(A), 086.A-0162(A), 086.A-0574(A), 087.A-0607(A), 088.A-0897(A), 091.C-

0934(B), 096.A-0095(A), 096.A-0418(A), 097.B-1070(A), 098.B-0537, 098.B-0537(A), 1103.A-0817, 294.A-5031(B), 60.A-9024(A).

DATA AVAILABILITY

The metal absorber catalogue used in this paper is publicly available and can be downloaded from this GitHub repository: <https://github.com/XQR-30/Metal-catalogue>.

REFERENCES

Anand A., et al., 2025, arXiv e-prints, p. arXiv:2504.20299

Asplund M., Grevesse N., Sauval A. J., Scott P., 2009, *ARA&A*, **47**, 481

Asthana S., Haehnelt M. G., Kulkarni G., Bolton J. S., Gaikwad P., Keating L. C., Puchwein E., 2024, arXiv e-prints, p. arXiv:2409.15453

Becker R. H., et al., 2001, *AJ*, **122**, 2850

Becker G. D., Rauch M., Sargent W. L. W., 2009, *ApJ*, **698**, 1010

Becker G. D., Bolton J. S., Lidz A., 2015a, *Publ. Astron. Soc. Australia*, **32**, e045

Becker G. D., Bolton J. S., Madau P., Pettini M., Ryan-Weber E. V., Venemans B. P., 2015b, *MNRAS*, **447**, 3402

Becker G. D., et al., 2019, *ApJ*, **883**, 163

Becker G. D., D'Aloisio A., Christenson H. M., Zhu Y., Worseck G., Bolton J. S., 2021, *MNRAS*, **508**, 1853

Berg T. A. M., et al., 2016, *Monthly Notices of the Royal Astronomical Society*, **463**, 3021

Bischetti M., et al., 2022, Widespread, strong outflows in XQR-30 quasars at the Reionisation epoch, doi:10.48550/arXiv.2205.00021

Bischetti M., et al., 2023, *ApJ*, **952**, 44

Bischetti M., et al., 2024, *ApJ*, **970**, 9

Bischetti M., Feruglio C., Carniani S., D'Odorico V., Salvestrini F., Fiore F., 2025, arXiv e-prints, p. arXiv:2504.15357

Boksenberg A., Sargent W. L. W., 2015, *ApJS*, **218**, 7

Bosman S. E. I., Becker G. D., Haehnelt M. G., Hewett P. C., McMahon R. G., Mortlock D. J., Simpson C., Venemans B. P., 2017, *MNRAS*, **470**, 1919

Bosman S. E. I., et al., 2022, *MNRAS*, **514**, 55

Cackett E. M., Miller J. M., Raymond J., Homan J., van der Klis M., Méndez M., Steeghs D., Wijnands R., 2008, *ApJ*, **677**, 1233

Calverley A. P., Becker G. D., Haehnelt M. G., Bolton J. S., 2011, *MNRAS*, **412**, 2543

Carrol B., Ostlie D., 2017, An Introduction to Modern Astrophysics. Addison Wesley

Codoreanu A., Ryan-Weber E. V., García L. Á., Crighton N. H. M., Becker G., Pettini M., Madau P., Venemans B., 2018, *MNRAS*, **481**, 4940

Cooper T. J., Simcoe R. A., Cooksey K. L., Bordoloi R., Miller D. R., Furesz G., Turner M. L., Bañados E., 2019, *ApJ*, **882**, 77

Crighton N. H. M., Prochaska J. X., Murphy M. T., O'Meara J. M., Worseck G., Smith B. D., 2019, *MNRAS*, **482**, 1456

D'Odorico V., et al., 2013, *MNRAS*, **435**, 1198

D'Odorico V., et al., 2016, *MNRAS*, **463**, 2690

D'Odorico V., et al., 2022, *MNRAS*, **512**, 2389

D'Odorico V., et al., 2023, *MNRAS*, **523**, 1399

Davies R. L., et al., 2023a, *MNRAS*, **521**, 289

Davies R. L., et al., 2023b, *MNRAS*, **521**, 314

Davies F. B., et al., 2024, *ApJ*, **965**, 134

Deepak S., Howk J. C., Lehner N., Péroux C., 2025, *ApJ*, **987**, 199

Díaz C. G., Ryan-Weber E. V., Karman W., Caputi K. I., Salvadori S., Crighton N. H., Ouchi M., Vanzella E., 2021, *MNRAS*, **502**, 2645

Doughty C., Finlator K., Oppenheimer B. D., Davé R., Zackrisson E., 2018, *MNRAS*, **475**, 4717

Fan X., et al., 2006, *AJ*, **132**, 117

Fan X., Bañados E., Simcoe R. A., 2023, *ARA&A*, **61**, 373

Faucher-Giguère C.-A., 2020, *MNRAS*, **493**, 1614

Ferland G. J., et al., 2017, *Rev. Mex. Astron. Astrofis.*, **53**, 385

Finlator K., Oppenheimer B. D., Davé R., Zackrisson E., Thompson R., Huang S., 2016, *MNRAS*, **459**, 2299

Fox A. J., et al., 2015, *ApJ*, **799**, L7

Fujimoto S., et al., 2019, *ApJ*, **887**, 107

Gaikwad P., et al., 2023, *MNRAS*, **525**, 4093

Gehrels N., 1986, *ApJ*, **303**, 336

Ginolfi M., et al., 2020, *A&A*, **633**, A90

Grevesse N., Asplund M., Sauval A. J., Scott P., 2010, *Ap&SS*, **328**, 179

Haardt F., Madau P., 2012, *ApJ*, **746**, 125

Harikane Y., et al., 2023, *ApJ*, **959**, 39

Kashino D., Lilly S. J., Matthee J., Eilers A.-C., Mackenzie R., Bordoloi R., Simcoe R. A., 2023, *ApJ*, **950**, 66

Keating L. C., Puchwein E., Haehnelt M. G., Bird S., Bolton J. S., 2016, *MNRAS*, **461**, 606

Kollmeier J. A., et al., 2014, *ApJ*, **789**, L32

Kramida A., Yu. Ralchenko Reader J., and NIST ASD Team 2024, NIST Atomic Spectra Database (ver. 5.12), [Online]. Available: <https://physics.nist.gov/asd> [2025, October 19]. National Institute of Standards and Technology, Gaithersburg, MD.

Lehner N., O'Meara J. M., Fox A. J., Howk J. C., Prochaska J. X., Burns V., Armstrong A. A., 2014, *ApJ*, **788**, 119

Lehner N., et al., 2022, *ApJ*, **936**, 156

Lewis J. S. W., et al., 2022, *MNRAS*, **516**, 3389

Madau P., Dickinson M., 2014, *ARA&A*, **52**, 415

Mason C. A., Chen Z., Stark D. P., Lu T.-Y., Topping M., Tang M., 2025, arXiv e-prints, p. arXiv:2501.11702

McQuinn M., 2016, *ARA&A*, **54**, 313

Mesinger A., Furlanetto S., 2009, *MNRAS*, **400**, 1461

Meyer R. A., Bosman S. E. I., Kakiichi K., Ellis R. S., 2019, *MNRAS*, **483**, 19

Muzahid S., 2014, *ApJ*, **784**, 5

Oyarzún G. A., et al., 2025, *ApJ*, **983**, 10

Pallottini A., Ferrara A., Gallerani S., Salvadori S., D'Odorico V., 2014, *MNRAS*, **440**, 2498

Péroux C., Howk J. C., 2020, *ARA&A*, **58**, 363

Perrotta S., et al., 2016, *MNRAS*, **462**, 3285

Pizzati E., Ferrara A., Pallottini A., Sommovigo L., Kohandel M., Carniani S., 2023, *MNRAS*, **519**, 4608

Pradeep J., Sankar S., Umasee T. M., Narayanan A., Khaire V., Gebhardt M., Sameer Jane C. C., 2020, *MNRAS*, **493**, 250

Puchwein E., Haardt F., Haehnelt M. G., Madau P., 2019, *MNRAS*, **485**, 47

Qin Y., et al., 2024, arXiv e-prints, p. arXiv:2412.00799

Rauch M., Sargent W. L. W., Womble D. S., Barlow T. A., 1996, *ApJ*, **467**, L5

Runnholm A., et al., 2025, *ApJ*, **984**, 95

Ryan-Weber E. V., Pettini M., Madau P., Zych B. J., 2009, *MNRAS*, **395**, 1476

Ryden 2017, Introduction to cosmology, 2nd edn. Cambridge University Press

Sadoun R., Zheng Z., Miralda-Escudé J., 2017, *ApJ*, **839**, 44

Satyavolu S., Kulkarni G., Keating L. C., Haehnelt M. G., 2024, *MNRAS*, **533**, 676

Schaye J., 2001, *ApJ*, **559**, 507

Sebastian A. M., et al., 2024, *MNRAS*, **530**, 1829

Simcoe R. A., et al., 2011, *ApJ*, **743**, 21

Songaila A., 2001, *ApJ*, **561**, L153

Songaila A., Cowie L. L., 2010, *ApJ*, **721**, 1448

Tang M., Stark D. P., Topping M. W., Mason C., Ellis R. S., 2024, *ApJ*, **975**, 208

Tumlinson J., Peeples M. S., Werk J. K., 2017, *ARA&A*, **55**, 389

Vernet J., et al., 2011, *A&A*, **536**, A105

Vito F., Di Mascia F., Gallerani S., Zana T., Ferrara A., Carniani S., Gilli R., 2022, *MNRAS*, **514**, 1672

Witstok J., et al., 2025, *Nature*, **639**, 897

Wolfe A. M., Turnshek D. A., Lanzetta K. M., Lu L., 1993, *ApJ*, **404**, 480

Zhu Y., et al., 2021, *ApJ*, **923**, 223

Zhu Y., et al., 2022, *ApJ*, **932**, 76

Zhu Y., et al., 2023, *ApJ*, **955**, 115

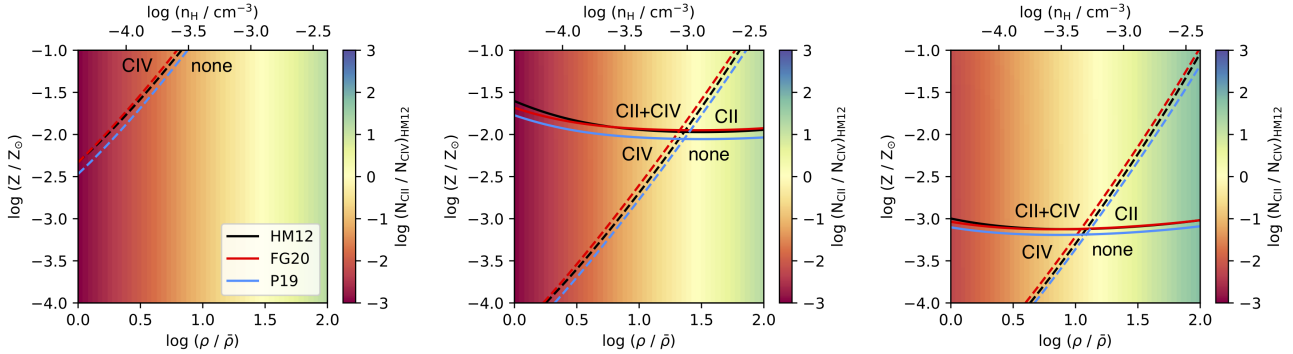


Figure A1. Effect of changing the UV background model on the detection regions for C II and C IV absorbers. All models are shown at redshift 5. The different panels show 10^{15} cm^{-2} (left), 10^{17} cm^{-2} (middle) and 10^{19} cm^{-2} (right). The black line is the Haardt & Madau (2012) model, the red line is the Faucher-Giguère (2020) model and the blue line is the Puchwein et al. (2019) model. The background color map shows the $N_{\text{CII}}/N_{\text{CIV}}$ ratio assuming the Haardt & Madau (2012) model for reference. As in Figure 6, the marked quadrants indicate the detectability of C II and C IV absorption: C II-only, no detection, C IV-only, and C II + C IV.

APPENDIX A: IMPACT OF UV BACKGROUND MODEL ON PROPERTIES OF DETECTABLE IONS

Throughout this work, we have explored the evolution of the $N_{\text{CII}}/N_{\text{CIV}}$ ratio using the Haardt & Madau (2012) model for the shape and amplitude of the UV background. However, the relative abundance of carbon ions is sensitive to the details of the UV background model (Finlator et al. 2016; Keating et al. 2016). We have therefore also explored the effect of alternative UV background models on the C II and C IV fractions we predict for a given gas density and metallicity. We consider here the Puchwein et al. (2019) and Faucher-Giguère (2020) models. The difference between these models and Haardt & Madau (2012) is an updated treatment of the IGM opacity during reionization, such that the models were designed to give a sensible evolution of the overall ionized hydrogen and helium fractions. They may therefore underestimate the number of photons with energies above the H I and He I ionization thresholds before hydrogen reionization is complete, and photons with energies above the He II ionization threshold before helium reionization is complete. For this reason we have used the Haardt & Madau (2012) model throughout this work, although as we will show all models produce similar results at fixed H I column density at this redshift. However, we note that this similarity may be because we are considering models at $z = 5$, after hydrogen reionization has completed but before AGN dominate the UVB.

We repeat the Cloudy modelling as described in Section 4 and the results are shown in Figure A1. We find that the positions of the C II and C IV detection contours are relatively insensitive to the choice of UV background model. This is due to our choice to fix the H I column density for a given hydrogen number density. This allows us to compensate with a change in the amplitude of the UVB with a change in the size of the absorber, to achieve a constant ionization parameter. Although these three models predict different amplitudes for the UV background at a given redshift, once the H I column density is fixed, the differences in the intensity of the UV background as a function of wavelength become more relevant. Above redshift 4, all of these models are dominated by star-forming galaxies, so their shapes are relatively similar. However, the *James Webb Space Telescope* has identified a population of faint AGN candidates into the EoR (e.g., Harikane et al. 2023). If these faint AGN contribute to reionization (Asthana et al. 2024), this may lead to more hard C IV-producing photons than are included in the UVBs investigated here, which could impact our modelled $N_{\text{CII}}/N_{\text{CIV}}$ ratio.

This paper has been typeset from a $\text{\TeX}/\text{\LaTeX}$ file prepared by the author.